

Research Article

First-Principles Calculations to Investigate Structural, Electronic, Optical, and Elastic Properties of Ceria

Lemessa Asefa Eressa ¹ and Teshome Gerbaba Edossa ²

¹Department of Physics, College of Natural & Computational Sciences, Ambo University, Ambo, Ethiopia

²Departments of Physics, College of Natural & Computational Sciences, Wachemo University, Hossana, Ethiopia

Correspondence should be addressed to Lemessa Asefa Eressa; lemessaphys@gmail.com

Received 16 January 2022; Accepted 25 April 2022; Published 3 June 2022

Academic Editor: Raouf El Mallawany

Copyright © 2022 Lemessa Asefa Eressa and Teshome Gerbaba Edossa. This is an open access article distributed under the Creative Commons Attribution License, which permits unrestricted use, distribution, and reproduction in any medium, provided the original work is properly cited.

The structural, electronic, optical, and elastic properties of Ceria (CeO_2) were investigated using local density approximation (LDA), PBE, DFT + U , and PBE0 approximations. In all approximations, the convergence test of total energy with respect to kinetic energy cutoff, k-point, and lattice constant of CeO_2 was performed consequently to increase the accuracy of computations. The O (2p)-Ce (4f) bandgap of CeO_2 calculated using DFT + U (3.0 eV) is consistent with experimentally reported value (3.0–3.33 eV) than with LDA (2.2 eV), PBE (2.5 eV), and PBE0 (4.47 eV). Both LDA and PBE underestimated the bandgap of CeO_2 while the PBE0 overestimated the bandgap of CeO_2 as compared to the experimental value. The optical properties such as the imaginary part of the dielectric function (ϵ_2), extinction coefficient (k), and refractive index (n) of ceria obtained using the three approaches are also consistent with the available theoretical and experimental data. In addition, the maximum peak for absorption coefficient was found at about 13 eV for (LDA and PBE) and around 11 eV for DFT + U calculations. Furthermore, the analyses of optical properties support the electronic properties of ceria. The elastic properties such as bulk modulus, shear modulus, Young's modulus, Poisson's ratio, Debye temperature, and Debye sound velocity were computed to investigate the mechanical properties of CeO_2 and compared with the experimental and theoretical results. The result of elastic parameters found confirms that CeO_2 is mechanically stable and has potential for a variety of different electronic applications.

1. Introduction

Ceria (CeO_2) is a technologically significant oxide material that has a wide range of applications. It is widely used in automotive three-way catalysts (TWCs) to remove NOx and CO [1], in luminescence devices, gas sensors, and high-temperature superconducting tapes [2], as a catalyst in fuel cells [3–5]. Ceria is a highly correlated material, due to the fact of their confined d- and f-orbitals, where Coulomb repulsion energy acts on them on the order of the electronic bandwidth [1, 6]. Only a few researches have been carried out with density functional theories to define the needed properties of CeO_2 . Therefore, it is important to investigate the properties of ceria for the advancement of their practical applications with different density functional theories.

The local density approximation (LDA) or PBE underestimates and fails to reproduce the correct electronic properties (bandgap) of CeO_2 due to the f-electron delocalization associated with the self-interaction problem [7]. However, the electronic structure of CeO_2 is fundamental to understanding the effects of ions, doping, and other properties that are prerequisites to using CeO_2 for different technological applications. Hence, in order to account for the strong on-site Coulomb repulsion among the Ce-4f electrons, a Hubbard parameter U is added (DFT + U approach) so as to get better electronic properties. The objective of this study was to investigate the structural, electronic, optical, and mechanical properties of CeO_2 using density functional theories. The values obtained were compared with the available theoretical and experimental data.

2. Computational Methods

Structural, electronic, optical, and elastic properties of CeO₂ were computed by using density functional theory as implemented in the Quantum ESPRESSO (QE) open-source package. The exchange correlation is described by local density approximation (LDA) [8, 9], and the generalized gradient approximation (GGA) with the Perdew–Burke–Ernzerhof (PBE) functional calculations was employed [10, 11]. Moreover, the DFT + *U* approach was used with the Hubbard parameter (*U* = 5 eV) in order to accurately describe the energy bandgap and to avoid the underestimation error of LDA and PBE. To obtain accurate structural and electronic properties, the optimized kinetic energy cutoff, *k*-point, and lattice parameter optimizations were performed using LDA, PBE, and DFT + *U* calculations. The optical properties were calculated using density functional perturbation theory. LDA, PBE, and DFT + *U* approaches were employed to calculate the structural, electronic, optical, and elastic properties of CeO₂. Moreover, the band structure of CeO₂ is also computed with a hybrid functional approximation (PBE0) [7]. Finally, the analysis of the structure, electronic, optical, and elastic properties of CeO₂ was compared with the theoretical and experimental data.

2.1. Structural Optimization. CeO₂ has a fluorite structure with space group Fm3m; it consists of a simple cubic oxygen sublattice with the Ce ions occupying alternate cube centers [7]. The relaxed structure is as shown in Figure 1(a). In order to achieve the equilibrium structure, one has to calculate the lattice parameter that minimizes the DFT total energy. The result of calculations performed for lattice parameter optimization with LDA, PBE, and DFT + *U* is described as shown in Figure 1(b).

Figure 1(b) shows the plot of lattice parameter CeO₂ calculated using LDA, PBE, and DFT + *U* approaches. The optimized lattice parameters of CeO₂ calculated with LDA, PBE, and DFT + *U* approaches are 5.407 Å, 5.418 Å, and 5.425 Å, respectively, and are in agreement with previous values reported in literature [3, 12–14]. The value of the optimized lattice parameter calculated with DFT + *U* is greater than in LDA and PBE and is consistent with previously reported literature [3]. These lattice parameters are used in the subsequent calculations for the respective approximating approach.

2.2. Electronic Properties of CeO₂. The density of states (DOS) helps to understand the behavior of state occupancy over specific energy intervals. It provides detail on the states that are unoccupied and the states that are occupied. A high DOS at a specific energy level describes the states available for occupation. However, there is no state occupied at DOS equal to zero. For CeO₂ the density of states is discontinuous for the width from the top of the valence band to the bottom of the conduction band that is normally the bandgap of the system.

Figures 2(a) and 2(b) show the corresponding band structure and density of states of CeO₂ using LDA

computation. The density of states described in Figure 2(b) is formed from the contributions of O2p (−4 eV–0 eV), Ce4f (2.2–4 eV), and Ce5d (6–10 eV), respectively. As shown in Figure 2(a), the bandgap of CeO₂ calculated with the LDA scheme between O2p to Ce4f and O2p to Ce5d is 2.2 eV and 6.0 eV, respectively.

Figures 3(a) and 3(b) show the corresponding band structures and density of states of CeO₂ calculated using PBE approximation, respectively. The density of states described in Figure 2(b) is formed from the contributions of O2p (−4 eV–0 eV), Ce4f (2.5–4 eV), and Ce5d (6–10 eV). Figure 3(a) depicts the bandgap of CeO₂ calculated with PBE approaches between O2p to Ce4f and O2p to Ce5d is 2.5 eV and 6.0 eV, respectively.

Figures 4(a) and 4(b) show the corresponding band structures and density of states of CeO₂ using DFT + *U* approximation. The density of states described in Figure 4(b) is formed from the contributions of O2p (−6 eV–1 eV), Ce4f (2–4 eV), and Ce5d (5–10 eV), respectively. Figure 4(a) indicates the bandgap of CeO₂ calculated with PBE approaches between O2p to Ce4f and O2p to Ce5d is 3.0 eV and 5.6 eV, respectively.

As can be seen in Figures 2(a), 3(a), 4(a), and 5, the O2p–Ce4f bandgap of CeO₂ obtained using LDA, PBE DFT + *U*, and PBE0 calculations is 2.2 eV, 2.5 eV, 3.0 eV, and 4.47 eV, respectively. The LDA and PBE approximations underestimated, whereas the PBE0 overestimated the O2p–Ce4f bandgap of CeO₂ compared to the experimental value (3.0–3.33 eV) [1, 15]. However, the DFT + *U* approximation is more consistent with the experimental value. The values of the O2p–Ce5d bandgap of CeO₂ calculated in the LDA, PBE, and DFT + *U* approaches are in the range of previous findings and experimental value of 5.5–8.0 eV [3, 7, 16]. The calculated bandgap of ceria with LDA, PBE, DFT + *U*, and PBE0 is summarized in Table 1 and compared with the experimental results.

As can be seen in Figures 6(a)–6(c), PDOS analysis shows that structure I is due to hybridization between O (2s) and Ce (3p) states, while the peaks in structure II result mainly from hybridization between O (2p) and Ce (5d) and also with some contributions of Ce (4f) states forming the valence band. The bottom of the conduction band is formed by localized and empty Ce (4f) states that are lower in energy than the empty Ce (5d) states. Structure III is highly localized due to hybridization between O (2p) states and Ce (4f) atomic states. The broad structure IV is mainly due to the hybridization of Ce (5d) states with O (2p) states. The empty and delocalized states V reflect the O2p-type states.

2.3. Optical Properties. The optical properties can be described from the dielectric function that gives the linear response of an electronic system submitted to an applied external electric field and can be written as follows [18]:

$$\epsilon(\omega) = \epsilon_1(\omega) + i\epsilon_2(\omega), \quad (1)$$

where the real part ($\epsilon_1(\omega)$) and the imaginary one ($\epsilon_2(\omega)$) describe, respectively, the dispersion and the absorption of the electromagnetic radiation by the medium which it

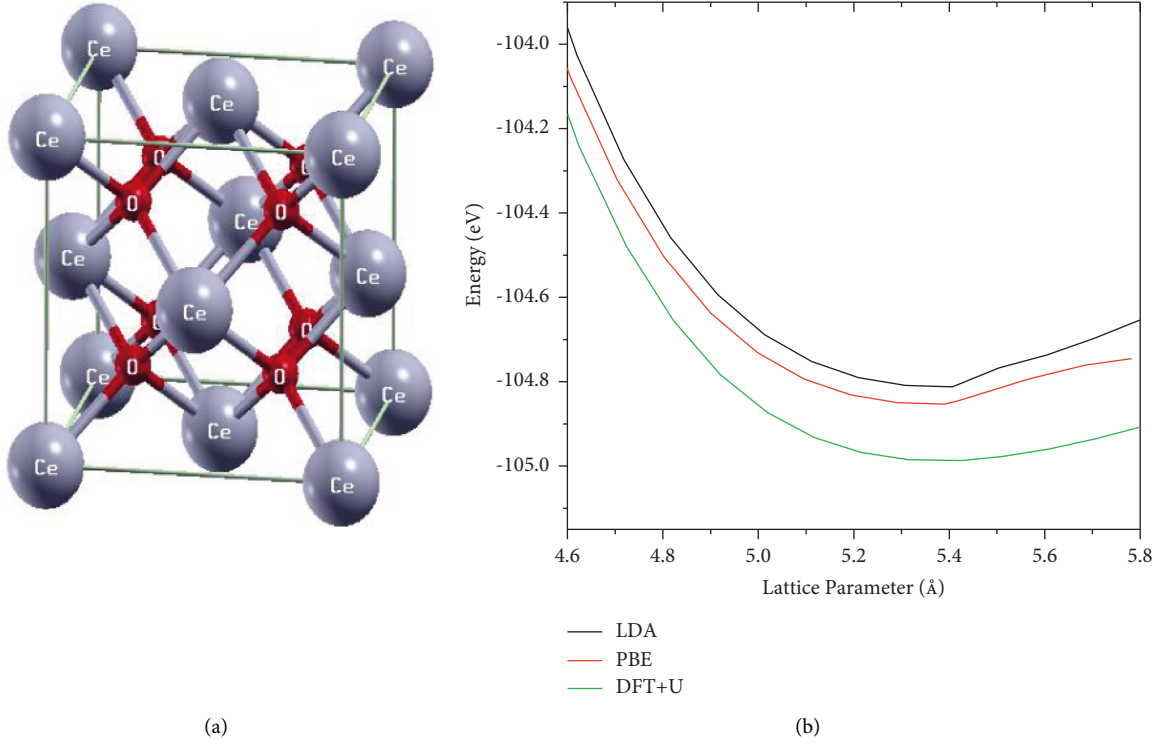


FIGURE 1: (a) Bulk structure of ceria and (b) lattice parameter of ceria in LDA, PBE, and DFT + U .

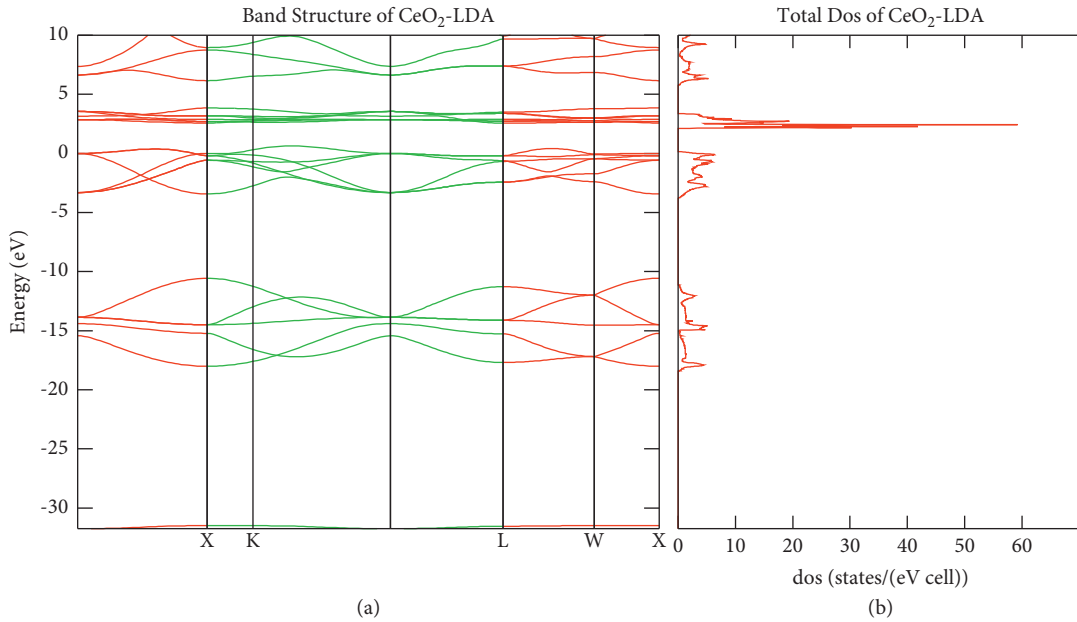


FIGURE 2: (a) Band structure of CeO_2 and (b) density of states of CeO_2 obtained with LDA.

crosses. $\epsilon_2(\omega)$ spectrum is calculated by summing the electric dipole operator matrix elements between the occupied and unoccupied wave functions over the Brillouin zone while respecting the selection rules [18]. This is mainly connected with the electronic structures and characterizes the linear response of the material to electromagnetic radiation. It therefore governs the propagation behavior of

radiation in a medium. The imaginary part $\epsilon_2(\omega)$ of the dielectric function represents the electron transition between the valence and the conduction bands. $\epsilon_2(\omega)$ is calculated by the following relation [19]:

$$\epsilon_2(\omega) = \left(\frac{4\pi^2 e^2}{m^2 \omega^2} \right) \sum_{ij} \int_{\text{BZ}} i|M|j|^2 F_i(1-F_j) \delta(E_F - E_i - \omega) d^3k, \quad (2)$$

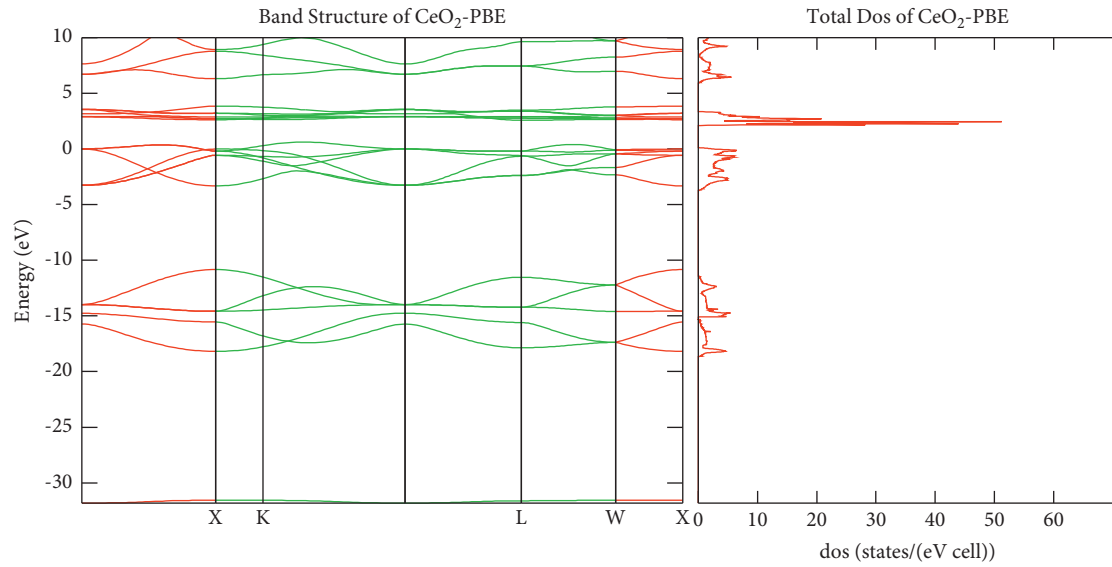


FIGURE 3: (a) Band structure of CeO₂ and (b) density of states of CeO₂ obtained with PBE approximations.

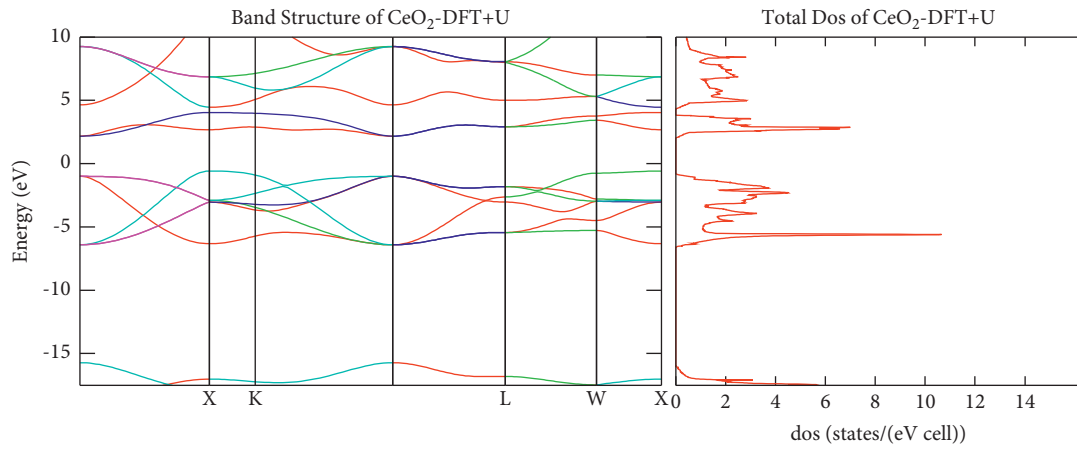


FIGURE 4: (a) Band structure of CeO₂ and (b) density of states of CeO₂ obtained with DFT + *U* approximations.

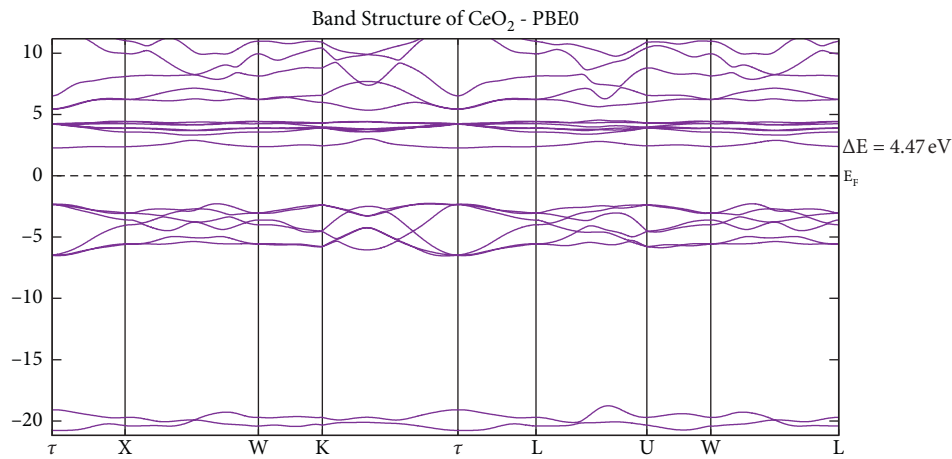
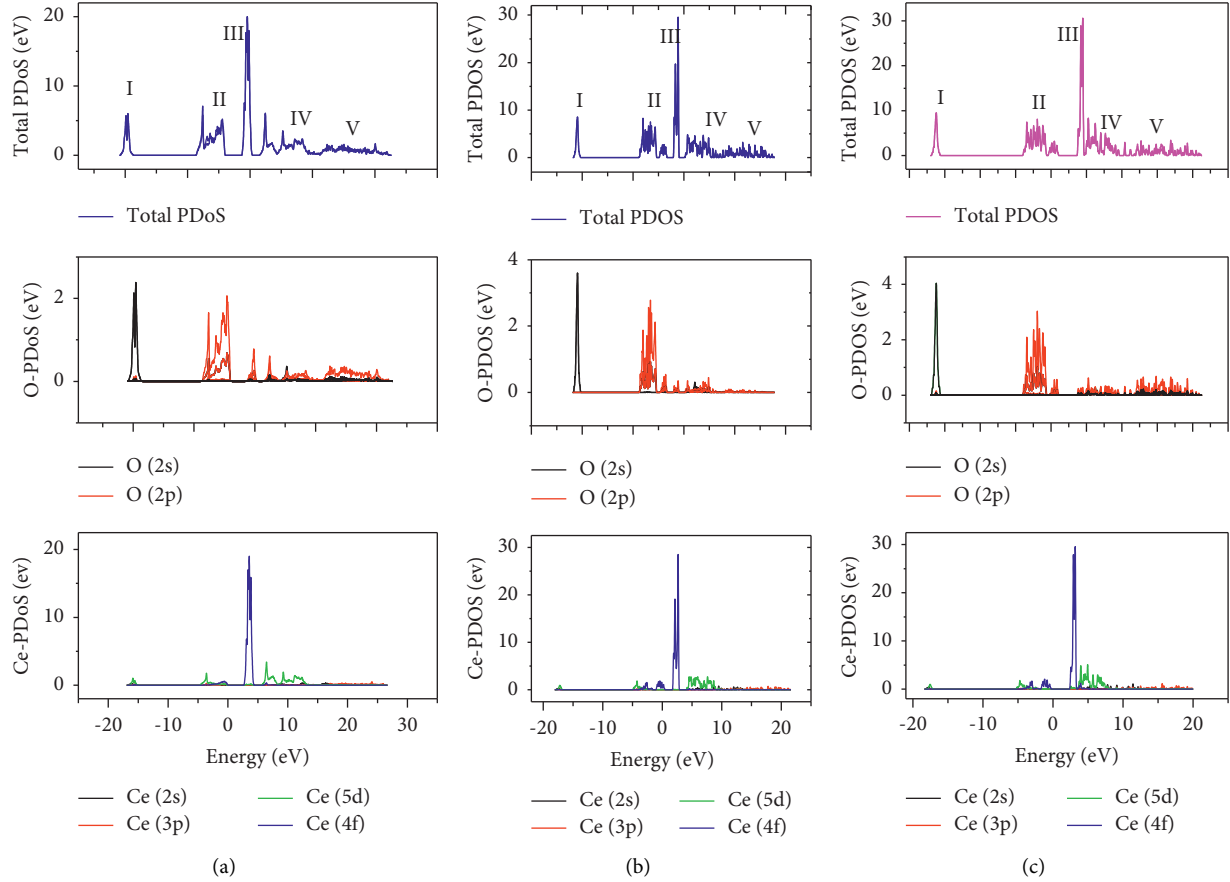


FIGURE 5: Band structure of CeO₂ obtained with PBE0 approximations.

TABLE 1: Calculated and experimental bandgap of ceria in (eV).

Approximation method	Energy bandgap of ceria in (eV)	
	O2p-Ce4f	O2p-Ce5d
LDA	2.2	6.0
PBE	2.5	6.0
DFT + U	3.0	5.6
PBE0	4.47	7.1
Experiment [1, 15, 17]	3.0–3.33	6–8

FIGURE 6: Partial density of states calculated with (a) LDA, (b) PBE, and (c) DFT + U .

where e is the electron charge; m is the free electron mass; ω is the frequency; i and j are the initial and final states, respectively; M represents the dipole matrix; F_i is the Fermi distribution function for the i -th state; and E_i is the energy of an electron in the i -th state. The dielectric function describes a causal response, so the real and imaginary parts are linked by a Kramers–Kronig transformation. The real part (ϵ_1) of the dielectric function can be extracted from the imaginary part using the Kramers–Kronig relation [19, 20] as follows:

$$\epsilon_1(\omega) = 1 + \frac{2}{\pi} P \int_0^{\infty} \frac{\omega' \epsilon_2(\omega')}{\omega'^2 - \omega^2} d\omega', \quad (3)$$

where ω is the frequency of the incident photons and P is the main part of the Cauchy integral. All other optical

parameters such as absorption coefficient $\alpha(\omega)$, refractive index $n(\omega)$, and reflection coefficient $R(\omega)$ can be derived from ϵ_1 and ϵ_2 .

$$n(\omega) = \left\{ \frac{\epsilon_1(\omega)}{2} + \frac{\sqrt{\epsilon_1^2(\omega) + \epsilon_2^2(\omega)}}{2} \right\}^{1/2}, \quad (4)$$

$$\alpha(\omega) = \sqrt{2\omega} \left[\sqrt{\epsilon_1^2(\omega) + \epsilon_2^2(\omega)} - \epsilon_1(\omega) \right]^{1/2}. \quad (5)$$

The following relation is obtained for the refractive index at low frequency and $x=0$:

$$n(0) = \epsilon(0)^{1/2}. \quad (6)$$

The reflection coefficient $R(\omega)$ characterizes the part of the energy that is reflected at the interface of the integral. It is given by [21]

$$R(\omega) = \left| \frac{\sqrt{\varepsilon(\omega)} - 1}{\sqrt{\varepsilon(\omega)} + 1} \right|^2. \quad (7)$$

The $L(\omega)$ optical parameter, called electron energy loss function, is an important parameter that describes the loss of energy when a fast-moving electron is traversing through a material, it is defined by

$$L(\omega) = \frac{\varepsilon_2(\omega)}{[\varepsilon_1^2 + \varepsilon_2^2]}, \quad (8)$$

and the extinction coefficient k is given by

$$k(\omega) = \frac{\left(-\varepsilon_1(\omega) + (\varepsilon_1^2(\omega) + \varepsilon_2^2(\omega))^{1/2} \right)^{1/2}}{\sqrt{2}}. \quad (9)$$

Figure 7(a) shows the real part $\varepsilon_1(\omega)$ of the dielectric function obtained by LDA, PBE, and DFT + U that is equivalent to Kramers–Kronig transformation and experimental result. The peak at about 2.5 eV corresponds to the experimental one at 3.12 eV, and the second broad peak of $\varepsilon_1(\omega)$ is situated at about 8 eV, corresponding to the experimental peak at 7.32 eV for LDA and PBE calculations [7]. However, the first peak was observed at 5 eV for DFT + U .

The calculated ε_2 curve in Figure 7(b) shows a sharp peak at about 3.5 eV for LDA and PBE and at about 7 eV for DFT + U . The second main peak is situated at about 11 eV, and the third one is situated at 21 eV for LDA and PBE. However, in DFT + U calculations, the second and third peaks were obtained at about 9 and 10 eV, respectively. The peaks of $\varepsilon_2(\omega)$ originate from interband transitions from valence band state to conduction band states. Consistent with the DOS of CeO₂, the first peak in ε_2 at about 3.5 eV is explained as the transition from Ce-5d to Ce-4f states, while the second peak corresponds to the Ce-5p → Ce-5d transition as described in DOS plot of CeO₂ (Figures 2(b), 3(b), and 4(b)). The width of the first peak in ε_2 depends on the width of the highest occupied valence band of CeO₂ as shown in Figures 2(b), 3(b), and 4(b).

The behaviors of optical properties for CeO₂ obtained with LDA, PBE, and DFT + U approximations were described in Figures 7(a)–7(e), 8(a), and 8(b).

The narrowband (Figure 7(b)) at around 3.5 eV (for LDA and PBE) and at 7 eV (for DFT + U) is associated with the transitions between occupied Ce (5d) states of the DOS structure II and the empty Ce (4f) states of the DOS structure III described on Figures 6(a)–6(c), respectively. The DOS structure II is mainly formed by the O (2p) states and the empty Ce (4f) states that are forbidden within the dipolar selection rule and do not contribute to the first peak of the calculated ε_2 .

The wide structure (Figure 7(b)) found between 11 eV and 15 eV on all approaches is primarily for transitions between O (2p) and Ce (5d) at energy intervals of 5 to 0 eV

(Figures 6(a) and 6(c)). Similarly, wideband is found between the Ce (5p) and Ce (5d) states in the energy interval 10 to 15 eV as indicated in Figures 6(a)–6(c). There is a good agreement between experimental and theoretical peak intensities, especially in the UV-vis region (peak I), but there are some differences at high energies. Figures 7(c) and 7(d) show the refractive index n and the extinction coefficient k of CeO₂, which is the real and imaginary part of the complex index of refraction $N(N = n + ik)$ related to the Kramers–Kronig transformation. They are obtained from the dielectric function by equations (4) and (9).

In the UV-vis region, there is a good agreement between measurements and calculation since the intensities of the peaks of ε_2 and the k spectra evolve identically ($\varepsilon_2 = 2nk$). Studies from the determined intensity variation of the ε_2 structure apply to the k -spectrum of three structures centered around approximately 3.5, 11, and 21 eV for LDA and PBE calculations. The first structure has a higher stiffness at the absorption edge, which improves absorption in the UV-vis region. This effect may be related to the localized Ce (4f) state. The result is a high index of refraction for near UV energy (Figure 7(c); strong absorption gives a strong index of refraction). In fact, since n has the same shape as the derivative of k , the presence of an absorption peak causes a large change in the index of refraction.

As can be seen in Figures 7(a)–7(d), DFT + U overestimates the intensities of n and ε_1 in the range of 4–6 eV while the intensities of k and ε_2 in the range of 5–10 eV. Obviously, in the high energy range where the photon energy is above about 15 eV, the value of the imaginary part is very small and close to zero. This result suggests that above 15 eV, CeO₂ is transparent from the ultraviolet to the visible light region. As can be seen in Figure 7(c), the value of the refractive index (n_0) obtained for CeO₂ with LDA, PBE, and DFT + U is 2.6, 2.7, and 2.8, respectively. These values are greater than the experimental value (2.38) of refractive index (n_0) previously reported in literature [6]. It can be seen in Figure 7(d), the DFT + U overestimates the extinction coefficient k of CeO₂ between 5 and 10 eV than in LDA and PBE approximations. Moreover, Figure 7(e) indicates the overestimated reflectivity of CeO₂ for a wide range of energy values between 5 and 20 eV in DFT + U than in LDA and PBE approximations.

Figures 8(a) and 8(b) show the CeO₂ absorption coefficient and energy loss spectrum calculated using the LDA, PBE, and DFT + U calculations. As shown in Figure 8(a), the absorption coefficient of CeO₂ calculated by LDA and PBE and the energy loss spectrum of CeO₂ are almost the same. The main peaks of the absorption coefficient for CeO₂ calculated by the LDA and PBE approximations are obtained around 7.5, 10, 13, 16, 18, and 21 eV. In addition, the main peaks of the absorption coefficient for CeO₂ computed with DFT + U are found around 7, 8, 9, 11, 16.5, and 18 eV. The maximum peak for the absorption coefficient was found around 13 eV for (LDA + PBE) and around 11 eV for DFT + U calculations. As can be seen in Figure 8(b), the main peaks of the CeO₂ energy loss spectrum calculated by LDA and PBE are found at approximately 14.5, 16, 17.5, 19, and 21 eV. Similarly, the main peaks of the energy loss spectrum calculated by DFT + U are at about 14, 17, 18, and

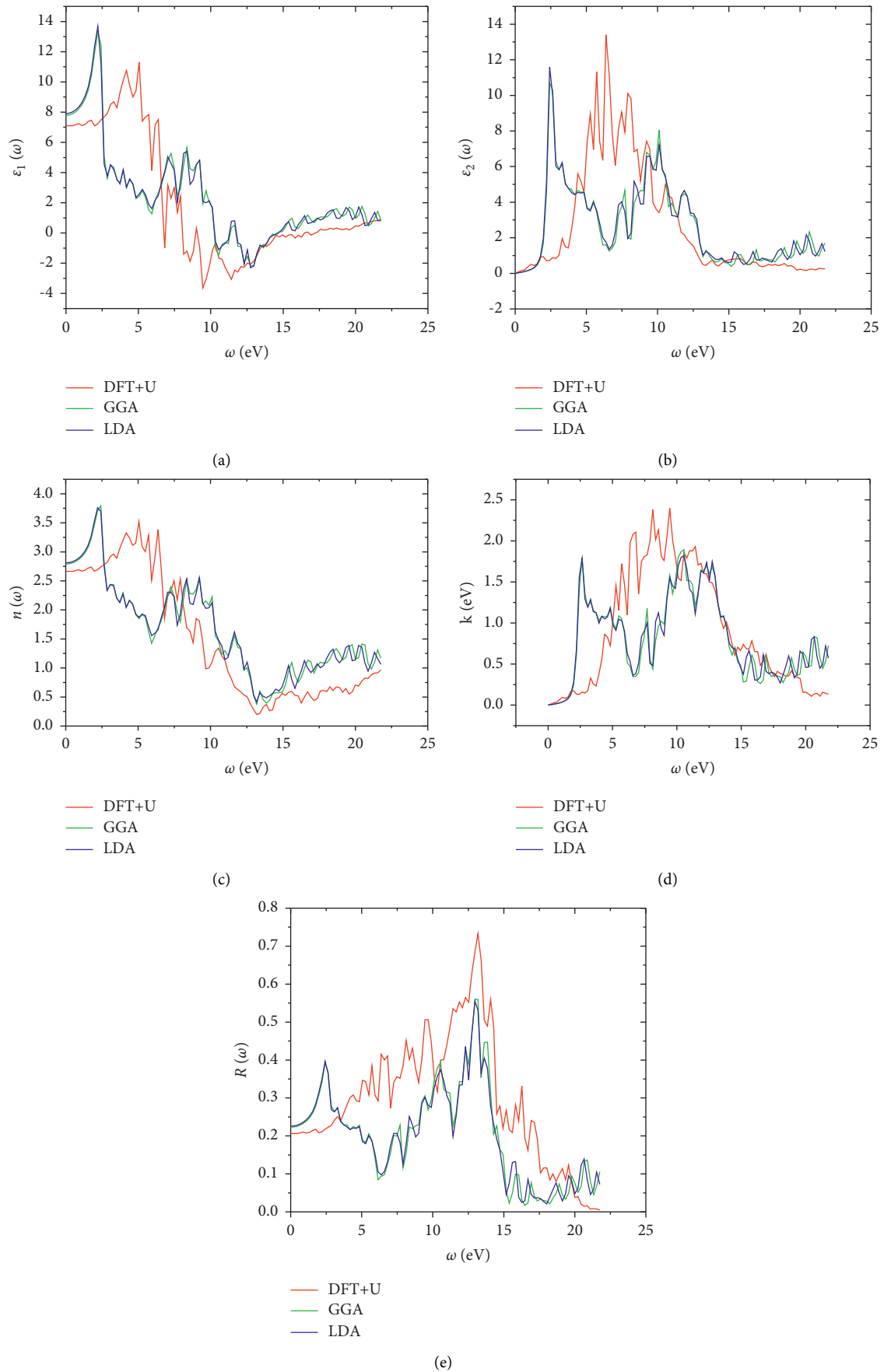


FIGURE 7: (a) Real dielectric function, (b) imaginary dielectric function, (c) refractive index, (d) extinction coefficient k , and (e) reflectivity of CeO₂.

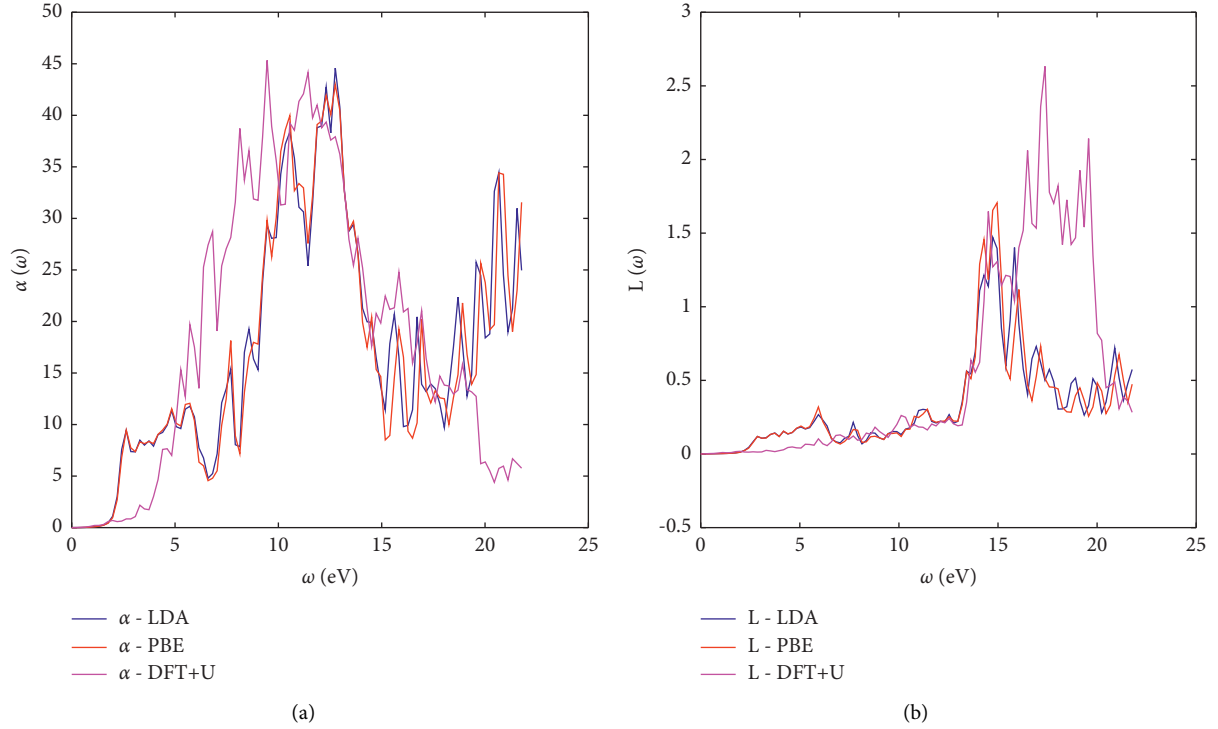


FIGURE 8: (a) Absorption coefficient and (b) energy loss of CeO_2 .

19.5 eV. The intensities of absorption coefficient and energy loss spectrum calculated with DFT + U were overestimated in the energy range (14–16 eV) and (16–19.5 eV) compared to LDA and PBE calculations, respectively. In order to compare the obtained result of absorption coefficient and energy loss spectrum of CeO_2 , theoretical or experimental data was not found.

3. Elastic Properties

Mechanical properties play a great role in the design and application of materials. The mechanical properties of a material such as fracture strength, Young's modulus, shear modulus, and hardness determine the capability of a material to resist external or internal stresses [22–30]. The study of the mechanical behavior of CeO_2 is useful to identify its various technological applications. Hence, the mechanical properties of CeO_2 are based on its elastic constants, which indicate response to external forces. Therefore, the elastic constants of CeO_2 are important parameters of a material and can provide valuable information about the mechanical stability, bonding character between adjacent atomic planes, brittleness, ductility, stiffness, and anisotropic character [31]. There are six components of stress and a corresponding six components of strain for the general 3-D case. Thus, Hooke's law may be expressed as follows:

$$\begin{aligned}\sigma_i &= C_{ij}\varepsilon_j, \\ \varepsilon_i &= S_{ij}\sigma_j.\end{aligned}\quad (10)$$

The number of independent elastic constants in CeO_2 is three (3), that is, C_{11} , C_{12} , and C_{44} . With reference to

Born–Huang's lattice dynamic theory, the mechanical stability of a cubic system is based on the conditions expressed in equations (14) and (15) [32–34]:

$$\begin{aligned}C_{11} &> 0, \\ C_{44} &> 0, \\ C_{11} - C_{12} &> 0, \\ C_{11} + 2C_{12} &> 0, \\ C_{12} &< B < C_{11}.\end{aligned}\quad (11)$$

For an isotropic crystal, the expression that was used for computing the bulk modulus is as follows:

$$B = \frac{1}{3}(C_{11} + 2C_{12}).\quad (12)$$

Similarly, shear modulus, G is described by the following relation:

$$G = \frac{1}{2}(G_V + G_R),\quad (13)$$

where

$$G_V = \frac{(2C + 3C_{44})}{5},\quad (14)$$

$$G_R = \left(\frac{6}{C} + \frac{9}{C_{44}}\right)^{-1},\quad (15)$$

$$C = \frac{C_{11} - C_{12}}{2},\quad (16)$$

where G_V and G_R are Voigt shear modulus and Reuss shear modulus, respectively. Young's modulus E and Poisson's ratio n can be obtained in connection with the bulk modulus B and the shear modulus G as follows:

$$\begin{aligned} E &= \frac{9BG}{3B + G}, \\ n &= \frac{3B - 2G}{2(3B + G)}. \end{aligned} \quad (17)$$

The Debye temperature θ_D is proportional to the average elastic wave velocity v_a , and θ_D may be calculated from the average elastic wave velocity, v_a [35] given by [9]

$$\theta_D = \frac{h}{k_B} \left[\frac{3n}{4\pi V_0} \right]^{1/3} v_a, \quad (18)$$

where h is Planck's constant, k_B is Boltzmann's constant, V_0 is the volume of the unit cell, and n is the number of atoms in the unit cell.

The elastic constants are important parameters that provide information on the properties of a material such as stiffness, strength, mechanical stability, hardness, and ductility or brittleness [35]. As can be seen in Table 2, the elastic constants of CeO₂ computed using LDA, PBE, and DFT+ U approximations satisfy the Born's mechanical stability criteria $C_{11} - C_{12} > 0$, $C_{11} + 2C_{12} > 0$, and $C_{14} > 0$ [36]. That means CeO₂ is mechanically stable. The elastic constants are described in matrix format [35]. The elastic constants C_{ij} (in GPa) of CeO₂ calculated by (a) LDA, (b) PBE, and (c) DFT+ U are displayed in Matrixes (a), (b), and (c), respectively.

$$\begin{aligned} a &= \begin{pmatrix} 294.68 & 62.780 & 62.780 & 0.0000 & 0.0000 & 0.0000 \\ 62.780 & 294.68 & 62.780 & 0.0000 & 0.0000 & 0.0000 \\ 62.780 & 62.780 & 294.68 & 0.0000 & 0.0000 & 0.0000 \\ 0.0000 & 0.0000 & 0.0000 & 40.260 & 0.0000 & 0.0000 \\ 0.0000 & 0.0000 & 0.0000 & 0.0000 & 40.260 & 0.0000 \\ 0.0000 & 0.0000 & 0.0000 & 0.0000 & 0.0000 & 40.260 \end{pmatrix}, \\ b &= \begin{pmatrix} 307.51 & 78.870 & 78.870 & 0.0000 & 0.0000 & 0.0000 \\ 78.870 & 307.51 & 78.870 & 0.0000 & 0.0000 & 0.0000 \\ 78.870 & 78.870 & 307.51 & 0.0000 & 0.0000 & 0.0000 \\ 0.0000 & 0.0000 & 0.0000 & 41.440 & 0.0000 & 0.0000 \\ 0.0000 & 0.0000 & 0.0000 & 0.0000 & 41.440 & 0.0000 \\ 0.0000 & 0.0000 & 0.0000 & 0.0000 & 0.0000 & 41.440 \end{pmatrix}, \\ c &= \begin{pmatrix} 387.11 & 218.85 & 218.85 & 0.0000 & 0.0000 & 0.0000 \\ 218.85 & 387.21 & 218.85 & 0.0000 & 0.0000 & 0.0000 \\ 218.85 & 218.85 & 387.21 & 0.0000 & 0.0000 & 0.0000 \\ 0.0000 & 0.0000 & 0.0000 & 40.160 & 0.0000 & 0.0000 \\ 0.0000 & 0.0000 & 0.0000 & 0.0000 & 40.160 & 0.0000 \\ 0.0000 & 0.0000 & 0.0000 & 0.0000 & 0.0000 & 40.160 \end{pmatrix}. \end{aligned} \quad (19)$$

As can be seen in Matrixes (a), (b), and (c), the values of C_{11} computed using LDA, PBE, and DFT+ U are 294.68 GPa, 307.51 GPa, and 387.21 GPa, respectively. These values are in better agreement with previous theoretical results reported in literature (343 GPa) [2] and 26.8%, 23.69%, and 3.9% lower than the experimental value (403 GPa) [37] for LDA, PBE, and DFT+ U calculations, respectively. Moreover, the value of C_{12} computed with LDA, PBE, and DFT+ U is 62.78 GPa, 78.87 GPa, and 218.85 GPa, respectively. This value is underestimated for LDA and PBE and overestimated with DFT+ U calculations compared to the experimental result (105 GPa) [37] and reported result in literature (102 GPa) [2]. The values of C_{44} calculated with LDA, PBE, and DFT+ U approximations are 40.26 GPa, 41.44 GPa, and 40.16 GPa, respectively, and lower than the previously reported value in literature (55 GPa) [2] and experimental value (60 GPa) [37].

Table 2 depicts the value of bulk modulus, shear modulus, Young's modulus, Poisson's ratio, Debye sound velocity, and Debye temperature of CeO₂ obtained with LDA, PBE, and DFT+ U approaches in the Voigt-Reus-Hill average approximations model. The bulk moduli of CeO₂ found with LDA, PBE, and DFT+ U computations are 140.8 GPa, 155.08 GPa, and 274.97 GPa, respectively. The values of bulk modulus obtained with LDA and PBE approximations are lower than the reported experimental value (204 and 220 GPa) [37, 38] but near to the reported value in literature (124 and 174 GPa) [39, 40]. However, the value of bulk modulus of CeO₂ obtained with the DFT+ U approach is greater than the experimental value. Moreover, the value of the shear modulus of CeO₂ calculated with LDA, PBE, and DFT+ U are 62.51 GPa, 63.11 GPa, and 54.28 GPa, respectively. These values of shear modulus are also lower than previously reported experimental value (87 GPa) [37] and reported results in literature (76 GPa) [2]. The values of Young's modulus of CeO₂ found using LDA, PBE, and DFT+ U are 162.96 GPa, 166.48 GPa, and 152.75 GPa, respectively. These values of Young's modulus are less than previously reported experimental value (228 GPa) [37] and reported result in literature (200 GPa) [2]. But it is greater than previous reported results in literature (102.15 GPa) [32].

The Poisson's ratio is often utilized to measure the malleability of crystalline compounds [41]. Moreover, it provides information about the bonding forces characteristics that is a measure of compressibility, that is, it is a ratio of lateral to longitudinal strain in uniaxial tensile stress and is given by [42]:

$$n = \frac{C_{12}}{C_{11} + C_{12}}. \quad (20)$$

A material is characterized as brittle when the Poisson's ratio value is ($n \leq 1/3$) and as ductile materials when ($n \approx 1/3$) [2]. In this study, the Poisson's ratio obtained in all approximations is higher than the values previously reported in literature (0.293) [32]. As shown in Table 2, the Poisson's ratio of CeO₂ computed in this study is between

TABLE 2: Mechanical parameters of CeO₂.

Method	Approximation method			Experiment
	LDA	PBE	DFT + <i>U</i>	
Bulk modulus (GPa)	140.08	155.08	274.97	220 [38]
Young's modulus (GPa)	162.96	166.48	152.75	228 [37]
Shear modulus (GPa)	62.51	63.11	54.28	87 [37]
Poisson ratio (<i>n</i>)	0.30	0.31	0.40	0.293 [32]
Debye sound velocity (m/s)	3,200.07	3,231.59	3,076.84	—
Debye temperature (K)	395.48	399.37	380.25	489 [37]

0.3 and 0.4 constituting CeO₂ as ductile material. The Debye temperature value calculated with LDA, PBE, and DFT + *U* are 395.48 K, 399.37 K, and 380.25 K, respectively. These values are less than the experimental value (489 K) [37] and reported results in literature (462 K) [2]. But consistent with the result reported in literature (395.5 K) [43]. The Debye sound velocities computed are 3,200.07 m/s, 3,231.59 m/s, and 3,076.84 m/s with LDA, PBE, and DFT + *U* schemes, respectively. These values are nearly in agreement with the previously reported experimental and theoretical results [2, 37]. As seen in Table 2, all the mechanical parameters of CeO₂ computed with LDA, PBE, and DFT + *U* approximations were compared with available experimental results.

4. Conclusion

The structural, electronic, optical, and elastic properties of CeO₂ have been investigated using LDA, PBE, PBE0, and DFT + *U* (*U* = 5 eV) approaches. The calculated lattice parameter, bandgap, dielectric constants, refractive index, and extinction constant agree well with the available theoretical and experimental data. The bandgap of CeO₂ found using DFT + *U* calculation is more consistent with the experimental value than with LDA, PBE, and PBE0 approximations. The intensities of absorption coefficient and energy loss spectrum calculated using DFT + *U* were overestimated in the energy range of 14–16 eV and 16–19.5 eV compared to LDA and PBE calculations, respectively. The peaks of dielectric constants and refractive index of ceria obtained are consistent with the feature of the density of states properties found in the three scheme calculations. The obtained value of bulk modulus of ceria is underestimated in LDA and PBE whereas overestimated in DFT + *U* calculations compared to experimental results. The Young's and shear moduli values are underestimated in all approximations compared to experimental results. The Poisson's ratio is in good agreement with the experimental result.

Data Availability

All relevant data to this publications are included in the manuscript.

Conflicts of Interest

The authors declare that they have no conflicts of interest.

References

- [1] S. Shi, X. Ke, C. Ouyang et al., "First-principles investigation of the bonding, optical and lattice dynamical properties of CeO₂," *Journal of Power Sources*, vol. 194, no. 2, pp. 830–834, 2009.
- [2] P. F. Weck, P. A. Juan, R. Dingreville, and E. Kim, "Density functional analysis of fluorite-structured (Ce, Zr) O₂/CeO₂ interfaces," *Journal of Physical Chemistry C*, vol. 121, no. 27, pp. 14678–14687, 2017.
- [3] A. Kabir, S. S. Nishat, and S. Rahman, "The density functional theory (DFT) and DFT + *U* study of the effect of the on-site coulomb repulsion parameter *U* on the structural and magnetic properties of CeO₂ nanoparticles," *Bangladesh Journal of Physics*, vol. 27, no. 1, pp. 43–58, 2020.
- [4] L. A. Eressa and P. B. Rao, "Synthesis and characterization of ytterbium and samarium co-doped ceria as an electrolyte for intermediate-temperature solid oxide fuel cell application," *Materials Chemistry and Physics*, vol. 242, Article ID 121914, 2020.
- [5] J. R. Rostrup-Nielsen, "Catalytic steam reforming," *Catalysis*, Springer, vol. 5, pp. 1–117, Berlin, Germany, 1984.
- [6] M. E. Khalifi, F. Picaud, and M. Bizi, "Electronic and optical properties of CeO₂ from first principles calculations," *Analytical Methods*, vol. 8, no. 25, pp. 5045–5052, 2016.
- [7] J. Graciani, A. M. Marquez, J. J. Plata et al., "Comparative study on the performance of hybrid DFT functionals in highly correlated oxides: the case of CeO₂ and Ce₂O₃," *Journal of Chemical Theory and Computation*, vol. 7, no. 1, pp. 56–65, 2011.
- [8] M. Ameri, F. Bennar, S. Amel, I. Ameri, Y. Al-Douri, and D. Varshney, "Structural, elastic, thermodynamic and electronic properties of LuX (*X* = N, Bi and Sb) compounds: first principles calculations," *Phase Transitions*, vol. 89, no. 12, pp. 1236–1252, 2016.
- [9] Y. Benkaddour, A. Abdelaoui, A. Yakoubi et al., "First-principle calculations of structural, elastic, and electronic properties of intermetallic rare earth R₂Ni₂Pb (*R* = Ho, Lu, and Sm) compounds," *Journal of Superconductivity and Novel Magnetism*, vol. 31, no. 2, pp. 395–403, 2018.
- [10] S. P. Miller, B. I. Dunlap, and A. S. Fleischer, "Cation coordination and interstitial oxygen occupancy in co-doped zirconia from first principles," *Solid State Ionics*, vol. 227, pp. 66–72, 2012.
- [11] B. Fadila, M. Ameri, D. Bensaid et al., "Structural, magnetic, electronic and mechanical properties of full-Heusler alloys Co₂YA₁ (*Y* = Fe, Ti): first principles calculations with different exchange-correlation potentials," *Journal of Magnetism and Magnetic Materials*, vol. 448, pp. 208–220, 2018.
- [12] Y. Jiang, J. B. Adams, and M. Van Schilfgaarde, "Density-functional calculation of CeO₂ surfaces and prediction of

- effects of oxygen partial pressure and temperature on stabilities,” *The Journal of Chemical Physics*, vol. 123, no. 6, 2005.
- [13] M. Alaydrus, M. Sakae, and H. Kasai, “A DFT + U study on the contribution of 4f electrons to oxygen vacancy formation and migration in Ln-doped CeO₂,” *Physical Chemistry Chemical Physics*, vol. 18, no. 18, pp. 12938–12946, 2016.
- [14] J. L. F. Da Silva, M. V. Ganduglia-Pirovano, J. Sauer, V. Bayer, and G. Kresse, “Hybrid functionals applied to rare-earth oxides: the example of ceria,” *Physical Review B*, vol. 75, no. 4, Article ID 045121, 2007.
- [15] C. Loschen, C. Javier, K. M. Neyman, and F. I. Riera, “First-principles LDA + U and GGA + U study of cerium oxides: dependence on the effective U parameter,” *Physical Review B*, vol. 75, no. 3, Article ID 035115, 2007.
- [16] H. Yanagida, R. J. Brook, and F. A. Kröger, “Direct current voltage characteristics of calcia stabilized zirconia with porous platinum electrodes,” *Journal of the Electrochemical Society*, vol. 117, no. 5, p. 593, 1970.
- [17] J. L. F. Da Silva, M. V. Ganduglia-Pirovano, J. Sauer, V. Bayer, and G. Kresse, “Publisher’s note: hybrid functionals applied to rare-earth oxides: the example of ceria,” *Physical Review B: Condensed Matter*, vol. 75, no. 8, Article ID 089901, 2007.
- [18] A. Khireddine, A. Bouhemadou, S. Alnujaim et al., “First-principles predictions of the structural, electronic, optical and elastic properties of the zintl-phases AE₃GaAs₃ (AE = Sr, Ba),” *Solid State Sciences*, vol. 114, Article ID 106563, 2021.
- [19] I. Biziz, E. H. Atmani, N. Fazouan, and M. Aazi, “First-principles calculations of structural, electronic and optical properties of Cd_{1-x}Zn_xS ternary alloys,” *Surfaces and Interfaces*, vol. 24, Article ID 101126, 2021.
- [20] A. Bekhti-Siad, K. Bettine, D. P. Rai et al., “Electronic, optical and thermoelectric investigations of zintl phase AE₃AlAs₃ (AE = Sr, Ba): first-principles calculations,” *Chinese Journal of Physics*, vol. 56, no. 3, pp. 870–879, 2018.
- [21] T. Jiang, Q. He, M. Bi, X. Chen, H. Sun, and L. Tao, “First-principles calculations of adsorption sensitivity of Au-doped MoS₂ gas sensor to main characteristic gases in oil,” *Journal of Materials Science*, vol. 56, no. 24, pp. 13673–13683, 2021.
- [22] Y.-H. Park, T. Hinoki, and A. Kohyama, “Development of multi-functional NITE-porous SiC for ceramic insulators,” *Journal of Nuclear Materials*, vol. 386–388, pp. 1014–1017, 2009.
- [23] X. Fan, E. Case, F. Ren, Y. Shu, and M. Baumann, “Part II: fracture strength and elastic modulus as a function of porosity for hydroxyapatite and other brittle materials,” *Journal of the Mechanical Behavior of Biomedical Materials*, vol. 8, pp. 99–110, 2012.
- [24] J. E. Ni, F. Ren, E. D. Case, and E. J. Timm, “Porosity dependence of elastic moduli in LAST (lead-antimony-silver-tellurium) thermoelectric materials,” *Materials Chemistry and Physics*, vol. 118, no. 2-3, pp. 459–466, 2009.
- [25] F. Ren, E. D. Case, A. Morrison, M. Tafesse, and M. J. Baumann, “Resonant ultrasound spectroscopy measurement of young’s modulus, shear modulus and poisson’s ratio as a function of porosity for alumina and hydroxyapatite,” *Philosophical Magazine*, vol. 89, no. 14, pp. 1163–1182, 2009.
- [26] T. P. Hoepfner and E. Case, “The influence of the microstructure on the hardness of sintered hydroxyapatite,” *Ceramics International*, vol. 29, no. 6, pp. 699–706, 2003.
- [27] R. W. Rice, “Evaluation and extension of physical property-porosity models based on minimum solid area,” *Journal of Materials Science*, vol. 31, no. 1, pp. 102–118, 1996.
- [28] V. N. Kaliakin, *Introduction to Approximate Solution Techniques, Numerical Modeling, and Finite Element Methods*, CRC Press, Boca Raton, FL, USA, 2018.
- [29] A. Leyland and A. Matthews, “On the significance of the H/E ratio in wear control: a nanocomposite coating approach to optimised tribological behaviour,” *Wear*, vol. 246, no. 1-2, pp. 1–11, 2000.
- [30] J. Quinn and G. D. Quinn, “Indentation brittleness of ceramics: a fresh approach,” *Journal of Materials Science*, vol. 32, no. 16, pp. 4331–4346, 1997.
- [31] A. Mentefa, F. Z. Boufadi, M. Ameri et al., “First-principles calculations to investigate structural, electronic, elastic, magnetic, and thermodynamic properties of full-heusler Rh₂MnZ (Z = Zr, Hf),” *Journal of Superconductivity and Novel Magnetism*, vol. 34, no. 1, pp. 269–283, 2021.
- [32] J. C. Goldsby, “Basic elastic properties predictions of cubic cerium oxide using first-principles methods,” *Journal of Ceramics*, vol. 2013, Article ID 323018, 4 pages, 2013.
- [33] G. V. Sin’ko and N. A. Smirnov, “Ab initio calculations of elastic constants and thermodynamic properties of bcc, fcc, and hcp Al crystals under pressure,” *Journal of Physics: Condensed Matter*, vol. 14, no. 29, pp. 301–7005, 2002.
- [34] A. Moussali, M. B. Amina, B. Fassi, I. Ameri, M. Ameri, and Y. Al-Douri, “First-principles calculations to investigate structural and thermodynamic properties of Ni₂Laz (Z = As, Sb and Bi) Heusler alloys,” *Indian Journal of Physics*, vol. 94, no. 11, pp. 1733–1747, 2020.
- [35] H. Shao, X. Tan, J. Jiang, and H. Jiang, “First-principles study on the elastic properties of Cu₂GeSe₃,” *EPL (Europhysics Letters)*, vol. 113, no. 2, Article ID 26001, 2016.
- [36] M. Born, K. Huang, and M. Lax, “Dynamical theory of crystal lattices,” *American Journal of Physics*, vol. 23, no. 7, p. 474, 1955.
- [37] A. Nakajima, A. Yoshihara, and M. Ishigame, “Defect-induced raman spectra in doped CeO₂,” *Physical Review B: Condensed Matter*, vol. 50, no. 18, pp. 13297–13307, 1994.
- [38] J. Staun Olsen, L. Gerward, V. Kanchana, and G. Vaitheswaran, “The bulk modulus of ThO₂—an experimental and theoretical study,” *Journal of Alloys and Compounds*, vol. 381, no. 1-2, pp. 37–40, 2004.
- [39] K. Sato, H. Yugami, and T. Hashida, “Effect of rare-earth oxides on fracture properties of ceria ceramics,” *Journal of Materials Science*, vol. 39, no. 18, pp. 5765–5770, 2004.
- [40] K. Sato, K. Suzuki, K. Yashiro et al., “Effect of Y₂O₃ addition on the conductivity and elastic modulus of (CeO₂)_{1-x}(YO_{1.5})_x,” *Solid State Ionics*, vol. 180, no. 20–22, pp. 1220–1225, 2009.
- [41] I. Frantsevich, F. Voronov, and S. Bokuta, “Elastic constants and elastic moduli of metals and insulators,” *Naukova Dumka*, Kiev, Ukraine, 1983.
- [42] M. Ayad, F. Belkharroubi, F. Z. Boufadi et al., “First-principles calculations to investigate magnetic and thermodynamic properties of new multifunctional full-Heusler alloy Co₂TaGa,” *Indian Journal of Physics*, vol. 94, no. 6, pp. 767–777, 2020.
- [43] B. Zhu, Y. Cheng, Z. W. Niu, M. Zhou, and M. Gong, “LDA + U calculation of structural and thermodynamic properties of Ce₂O₃,” *Frontiers of Physics*, vol. 9, no. 4, pp. 483–489, 2014.